Reactive laser ablation in acetone towards phase-controlled nonequilibrium Iron- and Nickel-Bi2O3 nanoalloys

Reactive laser ablation in acetone towards phase-controlled nonequilibrium Iron- and Nickel-Bi_2O_3 nanoalloys

Ondřej Havelka[a,b,*], Sabrin Abdallah[a,b], Jan Braun[a], Dariusz tukowiec[c], Tomáš Plachý[d], Martin Cvek[d], Rafael Torres-Mendiet[a,*]

[a] *Institute for Nanomaterials, Advanced Technologies and Innovation, Technical University of Liberec, Studentská 1402/2, 461 17 Liberec, Czech Republic*

[b] *Faculty of Mechatronics, Informatics and Interdisciplinary Studies, Technical University of Liberec, Studentská 1402/2, 461 17 Liberec, Czech Republic*

[c] *Faculty of Mechanical Engineering, Silesian University of Technology, Konarskiego 18 a St., 44-100 Gliwice, Poland*

[d] *Centre of Polymer Systems, University Institute, Tomas Bata University in Zlín, Třída T. Bati 5678, 760 01 Zlín, Czech Republic*

** Corresponding authors. E-mail addresses: ondrej.havelka@tul.cz (O. Havelka), rafael.torres@tul.cz (R. Torres-Mendieta).*

ABSTRACT

The ongoing development of new nanocatalysts is powered by the ambitious vision of finely controlling their structure while ensuring their remarkable features in heterogeneous chemical reactions. Especially in processes where the catalysts must be recycled, the union of catalytic activity and magnetic motility belongs among the most desirable characteristics. In recent years, the effort to optimize this synergy in photocatalysis has led to a focus on creating bismuth-based bimetallic nanoparticles (NPs), also known as nanoalloys. Nevertheless, the optimization of their properties and sustainable development still need to be well-considered. Therefore, we herein present for the first time the synthesis of phase-controlled nickel-Bi_2 O_3 and iron-Bi_2O_3 NPs, whose non-equilibrium composition is provided by the sustainable method known as reactive laser ablation in liquids (RLAL), resulting in a bandgap modification in both types of magnetic nanoalloys. In addition, the profound analyses of RLAL introduce the first report about the limitations and new perspectives of this relatively novel nanotechnology, in which the usage of chemically similar magnetic foils (iron and nickel) leads to extensively different NPs compositions and properties. Overall, these findings provide a groundwork for understanding the formation of non-equilibrium nanoalloys representing a rising generation of nanocatalysts.

Keywords: Reactive laser ablation Magnetic nanoalloys Non-equilibrium nanoparticles Bi2O3 nanosheets Phase control

1. Introduction

The continuous incorporation of nanotechnology into our life has boosted the demand for rapid and efficient manufacturing of nanomaterials [1]. However, the hasty industrial transfer of the production methods, generally based on wet chemistry strategies [2,3], has gradually led to one of the most worrying ecological disasters of the last decade known as nanopollution [4,5]. This health risk is constantly growing with the ever-increasing introduction of by-products and waste into the

environment, which is generated as a consequence of using hazardous reducing and stabilizing agents. Furthermore, the environmental damage does not stop with the production of nanomaterials but escalates with its usage [6]. The most dramatic case is observed in nanoparticles (NPs), whose large surface-volume ratio fosters a remarkable interaction with the surrounding environment. In this way, if the NPs surface is plagued with waste material coming from the production itself, the waste will not only be released into the environment uncontrollably but will also lead to cross-chemical effects with the use of the NPs, thus, leading to their devaluation [7].

In response to such an issue, various NPs synthesis methods have been explored, such as those based on the use of chemicals whose by-products are either harmless or tend to be chemically inert [8]. These types of alternatives, commonly based on the use of natural derivatives (e.g., plant extracts and microorganisms), are however, very limiting in local raw material accessibility, complicated separation processes, low yield, and, especially, in the generation of NPs composed of only the selected elements [9]. Therefore, given the current trend of combining various properties in singular systems, whose most efficient representatives are NPs consisting of multiple elements [10], the scientific community searched for alternatives, among which, laser-mediated synthesis of nanomaterials notably stands out. In particular, reactive laser ablation in liquids (RLAL), which is a variation of the matured method known as laser ablation in liquids (LAL), [11,12] has been shown to be highly effective for this purpose [13].

In brief, the process consists of the laser-mediated ablation of a solid target immersed in a liquid medium filled with NPs precursor molecules, such as metal salts, enabling the formation of nanoalloys composed of elements from the ablated material and the precursors dispersed in the liquid. In principle, the out-of-equilibrium conditions exerted by the laser-matter interaction should enable the formation of nanoalloys, including all types of element combinations, even those that disagree with the four Hume-Rothery rules for constructing substitutional or interstitial solid solutions [14]. According to these rules, the combination of two distinct elements having a radii difference < 15%, matching crystalline structures, same valency, and similar electronegativity, should form homogenous substitutional nanoalloys [15]. On the other hand, those not conforming to the conditions would develop phase-segregated ones, such as core-shell NPs [16], Janus-like NPs [17], or nested NPs [18], among others.

Ideally, the sole analysis of these rules must be sufficient to predict the type of structure we could form. Nevertheless, as recently pointed out in various comprehensive reviews [13,19], the rapid cooling of coalescing nanostructured matter and its interaction with reactive species generated as a side effect of the ablation process leads to the formation of multi-phase NPs. Although this fact limits the technique in terms of custom design, it also provides separated nano-areas that can differ in chemical composition and crystalline structure, i.e., nonequilibrium nanoalloys. Since these are very appealing materials for various critical fields such as nanomedicine [20], microfiltration [21], bacterial eradication [22] or heterogeneous catalysis [23,24], and the out-ofequilibrium synthetic practices are increasingly widespread because of their versatility, it becomes crucial to expand the understanding of how the selection of elements influences the final structure of these nonequilibrium nanoalloys. As a result, we explored the implications of interchanging elements with similar physicochemical properties when generating materials that harness the synergistic properties arising from the union of two distinct elements. In this study, the model system to work with was recyclable photocatalysts due to their unique ability to capitalize on the combined advantages of both magnetic and photocatalytic properties. Since these properties are rarely found in single-element systems, their combination makes the model system particularly promising. In this context, Bi oxide magnetic nanoalloys were explored, because Bi is ubiquitous, exhibits low toxicity and high photocatalytic activity towards heterogeneous catalytic reactions like organic pollutant degradation, water splitting, and carbon dioxide reduction

[25]. Furthermore, Fe was chosen as one of the magnetic elements to complete this model as it is among the most commonly employed elements to provide Bi oxide photocatalysts with magnetophoretic motility, enabling an easy magnetically-driven separation from reaction mixtures [25,26]. For comparison, Ni was chosen as the other magnetic element since it has the closest physicochemical properties to Fe just after Co, but unlike this critical mineral, Ni carries a lower environmental impact, cost, and toxicity [27]. Moreover, as Karthi et al. [28] recently proved, combining it with Bi oxide species can improve their organic pollutant photocatalytic degradation performance.

Besides the impact of magnetic element exchange, this study also demonstrates that variations in the Bi precursor concentration during the synthesis provide an additional degree of freedom for engineering these NPs. The most critically altered aspects are oxidation, crystallinity, phase, and morphology, which ultimately lead to the formation of different types of Bi magnetic nanoalloys with finely-tuned properties, including bandgap position and magnetic saturation. Thus, the current findings contribute to the progress in understanding the limitations and opportunities in the laser-mediated synthesis of nanoalloys.

2. Methodology

Fig. 1 presents the basic setup scheme, indicating the experimental details. In brief, the metal foil (Fe with > 99.99% purity or Ni with > 99.98% purity, Sigma-Aldrich) was immersed in a liquid medium, which consisted of $Bi(NO_3)_3.5H_2O$ salt dispersed and continuously stirred by a magnetic stirrer in acetone (> 99.7% purity).

Table 1 List of samples subjected to various characterization techniques and their elemental compositions of magnetically-purified NPs.

Since little is known about the influence of salt concentration on the elemental composition of RLAL-mediated NPs, different salt concentrations (0, 0.001, 0.01, 0.1, 1, 10, and 100 mM) were tested. Once the salt was homogeneously dispersed in the liquid, the metal foil was irradiated. For that, a pulsed laser (Onefive Origami XP-S, NKT Photonics; pulse duration < 400 fs, central wavelength 1030 nm, and 3 mm beam diameter at the FWHM) with a maximum output power of 5.1 was used. To ensure the largest NPs production efficiency, a laser scanning head coupled to an F-theta scan lens (160 mm focal length) was employed to move the focused laser beam at 2 m/s through the metal foil surface in the lens focal plane in a raster-like pattern. The maximum NPs production rate was ensured by testing different repetition rates (RRs) and irradiation times (ITs) during the ablation process. The optimal values of 0.7 MHz and 20 min irradiation were then used for all samples (the optimization details are included in Fig. S1 in the Supplementary Material). Moreover, it is worth stating that the maximum NPs production rate was achieved at the fluence value of 0.07 J/cm^2, which slightly overpasses the Fe (~0.05 J/cm^2) [29] and Ni (~0.05 J/cm^2) [30] ablation thresholds, where electron heat diffusion length significantly decreases, and the ablation process occurs mainly due to phase explosion [31]. As described by Shih et al. [32] such a process principally leads to the formation of small (below 10 nm) NPs, which in RLAL, translates into an ideal surface-to-volume ratio for triggering the reduction of surrounding metal salts.

Although the laser parameters were optimized to consume all Bi salt during RLAL, the residual salt could still remain in the liquid after irradiation. Thus, these potential residues were removed through

the NPs centrifugation (Centrifuge MiniSpin plus, 15 min, 14500 rpm, 1.5 mL Eppendorf). After removing the supernatant, the sedimented NPs were re-dispersed in test tubes with fresh acetone by ultrasoni-cation (SONOREX DIGITEC DT 510 H, 35 kHz, 9.7 L). Subsequently, homogeneously dispersed NPs with a significant magnetic response were collected by a neodymium magnet (visualization of the cleaning process is included in the Supplementary Material (Fig. S2 A). This collection also served as a secondary cleaning procedure, removing unsuitable material for its potential future application, where magne-tophoretic motility would be needed. Mass and optical spectroscopes assessed the yield of magnetically-responsive semiconductor NPs and their elemental compositions (the ultraviolet-visible [UV-Vis] spectroscope Optima 2100Dv from Perkin Elmer was used to determine the NPs optical properties and the inductive coupled plasma mass spectroscope [ICP-MS] NexION 3000D from Perkin Elmer to measure the NPs element content), which can be found in Table 1.

Furthermore, the NPs morphology and element distribution were evaluated by scanning-transmission electron microscopy (S-TEM), employing a microscope (JTITAN 80-300, FEI) with a unique brightness field-emission gun X-FEG as a source of electrons, which is equipped with an energy-dispersive X-ray (EDX) detector (EDAX). The EDX data, TEM, high resolution TEM (HRTEM), and high-angle annular dark-field imaging (HAADF)-STEM images were collected at 300 kV.

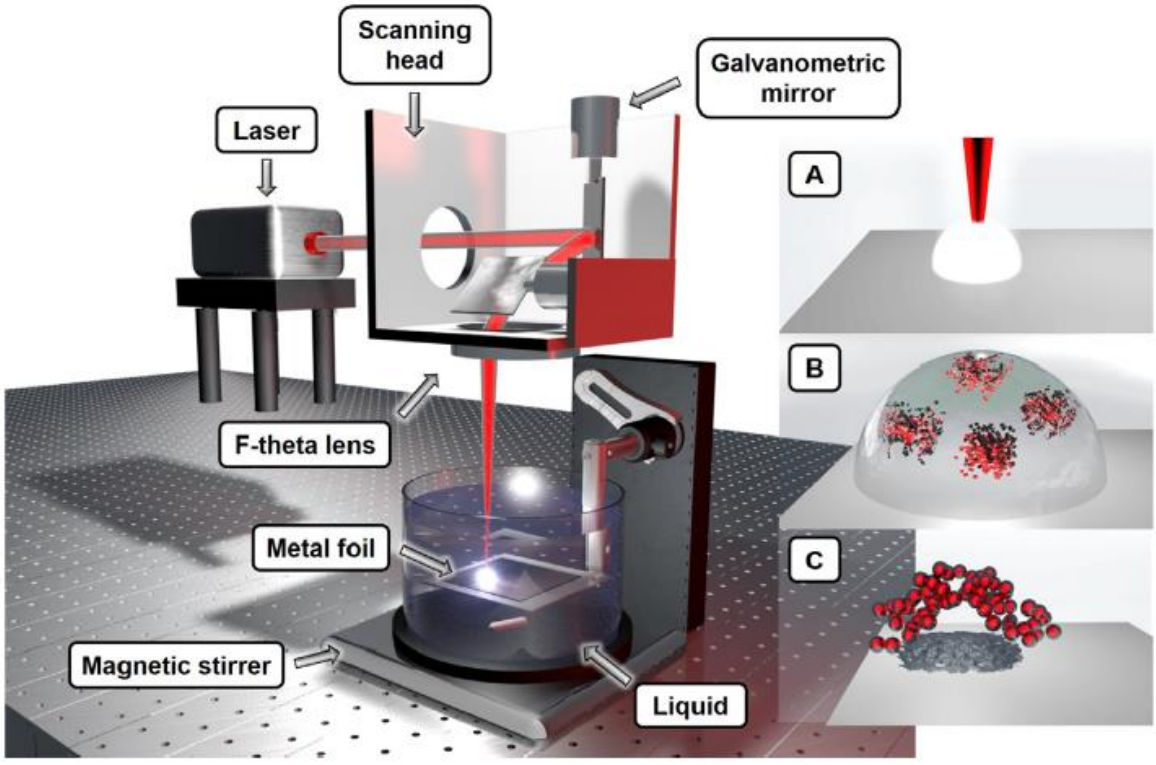

Fig. 1. Scheme representing the NPs preparation setup, including a general view of the laser scanning system, the F-theta lens, and irradiation of magnetic foil immersed in an acetone solution of $Bi(NO_3)_3.5H_2O$, which is magnetically stirred. The zoomed in figures represent (A) the initial irradiation of the magnetic foil during the laser ablation followed by (B) the creation of the cavitation bubble inside of which the interaction of bismuth and magnetic element atoms takes place. After the bubble collapse, (C) the formed bimetallic NPs are released into the surrounding liquid.

The same instrument was used to identify the crystallographic families by selected area electron diffraction (SAED). The NPs size distribution was assessed by manually measuring 500 particles for each sample employing the software ImageJ and the collected data of NPs sizes were fitted by a log-normal function with the general formula (1):

$$y(x) = \frac{1}{x\sigma\sqrt{2\pi}} e^{-\frac{(\ln x-\mu)^2}{2\sigma^2}} \quad (1)$$

where μ is the mean value and a is the standard deviation. In addition, the NPs crystallinity was confirmed by X-ray diffraction in powder (XRD) and by Raman spectroscopy. The XRD data was acquired by means of a diffractometer (Miniflex 600, Rigaku) operating at a wavelength of 0.1540 nm, in a 2θ angle range of 10-80°. The Raman data was collected with a Raman microscope (Nicolet DXR microscope, Thermo Scientific). The Raman spectra were analyzed through peak deconvolution, enabling chemical structure and phase identification. The mass magnetizations of the NPs were recorded by vibrating sample magnetometry (VSM) (Model 7404, Lake Shore) in external magnetic fields with a recording range ± 14.5 kOe. In detail, the analysis process was performed in a VSM sample holder (730931 Kel-F, powder up-per/bottom cup) mounted on a fiberglass tail under ambient conditions while the vibrating frequency, the amplitude of vibrations, and the time constant were set to 82 Hz, 1.5 mm, and 100 ms, respectively. To determine the bandgap energy, the Tauc plot transformation was employed, which was derived from UV-Vis measurements obtained within the wavelength range from 200 to 800 nm by using a UV-Vis spectrophotometer (PerkinElmer Lambda 35, Perkin Elmer, wavelength step 1 nm). Finally, the samples colloidal stability was assessed by laser Doppler-velocimetry (Zetasizer Nano ZS90, Malvern Instruments, laser wavelength centered at 633 nm) and UV-Vis spectroscopy (Hach-Lange, DR 3900, wavelength step 2 nm). Note that the NPs transfer into water for zeta potential measurements involved the substitution of acetone supernatant with demineralized water, followed by the sample centrifugation and subsequent addition of clean demineralized water (visualization of the NPs transfer process is included in the Supplementary Material Fig. S2 B). As acetone has a significantly larger dipole momentum than water (2.88 D and 1.85 D for acetone and water, respectively) [33], traces of acetone molecules or acetone degradation products can remain on the NPs surface, affecting their hydrodynamic stability compared to NPs without them.

3. Results

To date, parameters like laser fluence, pulse wavelength, pulse duration, solvent, or foil composition are known to control the NPs element content when employing the LAL method [13,19]. Among them, in the reactive variation RLAL, a new parameter comes into play; metal salt concentration, which has lately been employed to manipulate the element ratio in phase-segregated nanoalloys [21]. Nonetheless, the current study provides evidence that the range of salt concentrations for RLAL has limitations.

Unlike previous findings, high salt concentrations prevent the formation of NPs, specifically for 10 mM and 100 mM, which is demonstrated by the zero or close to zero concentration of magnetic elements in the samples found by ICP-MS. The decreased production in samples containing the highest salt concentration can result from the synergistic effect of viscosity increment, well-correlating with the inferior transportation of persistent bubbles during the ablation process resulting in bubble shielding [34], and the increment in laser beam absorption by the salt reaching ~50% for 10 mM samples (see Fig. S3 in the Supplementary Material); the insufficiently dissolved salt in the solvent hinders the delivery of laser light to the solid foil, as the employed fluence value is close to both solid targets' ablation thresholds, such an energy delivery blockage negatively impacts the ablation process reducing the production. Conversely, concentrations as low as 0.001 mM seem to disable the nanoalloy

formation, leading to the detected 100 wt% of the foil's element. Although Bi doping at the level of < 0.2 wt% cannot be completely ruled out due to the detection limits of the ICP-MS spectroscope (0.5 ppt) and the natural content of bismuth in the water, the low content of the doping element is far from the levels required in real applications for providing photosensitive semiconductor properties to the magnetic element. As a result, 0, 0.01, 0.1, and 1 mM samples are chosen for further examinations and are, thus, labeled according to Table 1, wherein their NPs elemental compositions are provided. Moreover, as not all Bi atoms coming from the employed salt amount can be efficiently incorporated into the NPs, Table 1 also shows the percentage of these unincorporated Bi atoms. These values in junction with the ICP-MS inspection of the disposed material in the cleaning process (24.3 wt%, 22.3 wt%, and 40.6 wt% for the $Ni_{Bi0.01}$, $Ni_{Bi0.10}$, and $Ni_{Bii0.10}$ samples and 20.1 wt%, 24.7 wt%, and 22.3 wt% for the $Fe_{Bi0.01}$, $Fe_{Bi0.10}$, and $Fe_{Bi1.00}$ samples, respectively) show that although RLAL is considered a sustainable synthetic process, its associated by-products can be substantial, especially when scaling up.

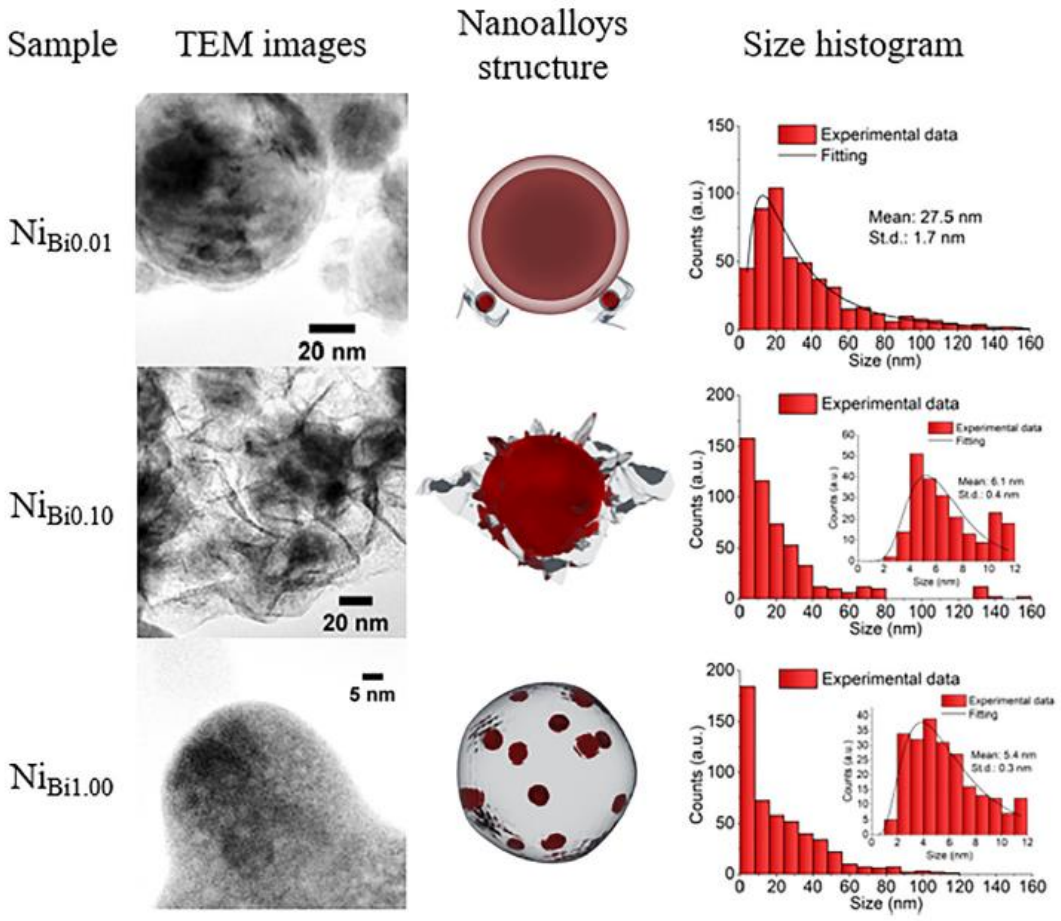

Fig. 2. Analysis of Ni-based samples displaying a size and morphology diversity In the NPs TEM Images. The Inset size histograms displayed for samples $Ni_{Bi0.10}$ and $Ni_{Bi1.00}$ represent the separate counting of very small NPs, which are either nested in bubble-like structures or around the nanostructure's perimeter. In the schematic nanoalloy structure visualization, red and gray colors represent noticeable phases in the NPs composition. Based on their contrast we are assuming, red corresponds to a Ni-based phase (the most dominant element according to ICP-MS data, except for $Ni_{Bi1.00}$ whose brightness evidences it is less abundant), and gray to a Bi-based one.

Table 2 Characteristic properties of the elements used for the preparation of bimetallic NPs.

Sample	Solid target	Salt concentration	Ni/Fe (wt%)	Bi (wt%)	Consumed Bi (wt%)
Ni		–	100	0	–
$Ni_{Bi0.01}$	Ni	0.01 mM	96.7 ± 0.7	3.3 ± 0.01	69.5
$Ni_{Bi0.10}$	foil	0.1 mM	80.6 ± 0.4	19.4 ± 0.04	74.0
$Ni_{Bi1.00}$		1 mM	5.8 ± 0.03	94.2 ± 0.8	47.9
Fe		–	100	0	–
$Fe_{Bi0.01}$	Fe	0.01 mM	95.8 ± 0.6	4.2 ± 0.02	76.8
$Fe_{Bi0.10}$	foil	0.1 mM	80.2 ± 0.8	19.8 ± 0.6	69.6
$Fe_{Bi1.00}$		1 mM	27.8 ± 0.2	72.2 ± 0.4	73.3

3.1. Morphology

The inspection of TEM images taken from multiple NPs per sample set shows key differences between Ni-based (Fig. 2) and Fe-based samples (Fig. 3). Despite employing foils with extremely similar basic physicochemical properties are used (Table 2), the same salt concentrations do not necessarily lead to identical morphologies. For instance, in the case of the $Ni_{Bi0.01}$ sample, the NPs have a bimodal size distribution characteristic of laser-mediated methodologies [35]. Moreover, both small and large NPs exhibit predominantly core-shell structures, which are occasionally covered by two-dimensional (2D) nanosheets. On the contrary, sample $Fe_{Bi0.01}$, whose Ni-based counterpart is $Ni_{Bi0.01}$ sample, shows fundamental differences. Although both samples exhibit small and large core-shell NPs (size 20-30 nm), the substantial morphological difference is the absence of the nanosheets. These discrepancies in Ni- and Fe-based samples become more pronounced as the amount of salt increases.

In the case of the $Ni_{Bi0.10}$ sample, a massive amount of nanosheets encapsulate spherical NPs, which are surrounded by clusters of smaller ones (mean size: 6.1 nm, Fig. S7 in the Supplementary Material). Unlike sample $Ni_{Bi0.01}$, the spherical NPs no longer exhibit a core-shell structure. For the Fe-based counterpart, FeBi010, although the coreshell structure is still visible, many small particles are also observed (mean size: 1.3 nm). This finding indicates that the 0.01-0.1 mM salt concentration range can be considered a threshold for creating predominantly small NPs in both Ni-based and Fe-based samples. Especially, the $Fe_{Bi0.10}$ exhibits the smallest mean size. Moreover, similar to previous reports indicating the formation of small NPs nested in larger ones as a consequence of non-equilibrium conditions associated with the laser synthesis methods [18], $Fe_{Bi0.10}$ sample also shows a nested-like structure.

Finally, the morphological changes are the most pronounced in the case of $Ni_{Bi1.00}$ and $Fe_{Bi1.00}$ samples. On the one hand, for the Ni-based samples, the NPs in $Ni_{Bi1.00}$ look considerably different from those observed in $Ni_{Bi0.01}$ and $Ni_{Bi0.10}$, which show an amorphous structure resembling nanobubbles that encapsulate small NPs (mean size: 5.4 nm). Considering that the only difference between all these samples is the amount of employed dopant, it is possible to assume that its abundance during the NPs creation can facilitate the tuning of the final morphology. For instance, when employing the lowest amount of dopant (sample $Ni_{Bi0.01}$), it seems to be inadequately incorporated into the NPs and rather covers the surface of Ni NPs, enabling the formation of core-shell NPs. hen increasing the dopant amount by one order of magnitude (sample $Ni_{Bi0.10}$), the dopant starts forming larger structures resembling 2D nanosheets that, although still covering the surface of Ni NPs, start acting as capping

agents. These capping agents block the natural heteroaggregation of small NPs over larger ones [36], which usually occurs in nanocolloids composed of ligand-free NPs that show a bimodal size distribution. hen increasing the dopant amount by an additional order of magnitude (sample NiBi100), the dopant no longer permits the NPs bimodal size distribution, suggesting that there is a limit to the dopant amount for which it begins to intervene so profoundly in the NPs formation process that size quenching occurs followed by encapsulation.

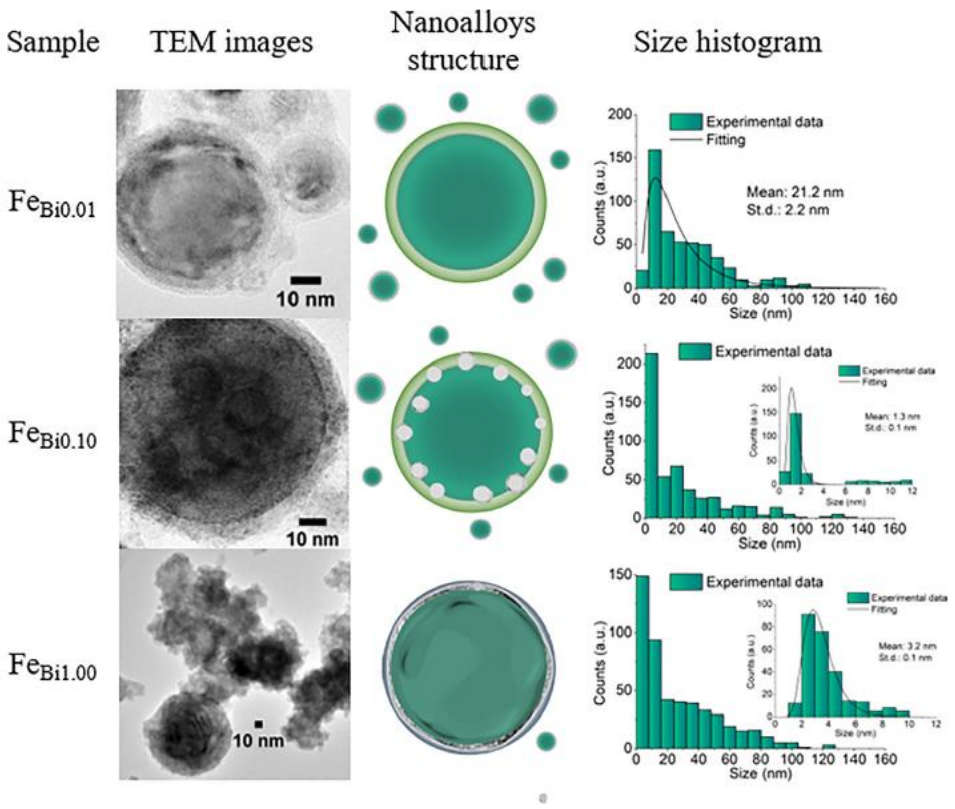

Fig. 3. Analysis of Fe-based samples displaying a size and morphology diversity in the NPs TEM images. The inset size histograms displayed for samples $Fe_{Bi0.10}$ and FeBlloo represent the separate counting of very small NPs, which either form part of bigger NPs or are located around the nanostructure's perimeter. In the schematic nanoalloy structure visualization, green and gray colors represent noticeable phases in the NPs composition. Based on their contrast we are assuming, green corresponds to a Fe-based phase (the most dominant element according to ICP-MS data, except for FeBu.oo whose brightness evidences it is less abundant), and gray to a Bi-based one.

In contrast to the behavior of Ni-based samples, when increasing the dopant concentration in Fe-based ones, the increment in the dopant amount seems to force the transformation from phase-segregated NPs into homogeneously mixed ones. Unlike the case of Ni-based NPs, Fe appears to incorporate more efficiently the Bi dopant into its structure. For instance, the fact that in $Fe_{Bi0.10}$, the 0.1 mM Bi salt does not lead to the formation of independent 2D nanosheets but rather a nested-like structure suggests the internalization of Bi dopant into the Fe NPs system. Moreover, the shell suppression in FeBi100 and contrast homogenization in the corresponding TEM micrographs, which evidences no significant element segregation, points to a more proper Bi internalization and distribution within the NPs. Even though according to the first Hume-Rothery rule, the large difference in atomic radii would not allow the formation of substitutional alloys, neither for Bi/Ni (atomic radii difference of 25.2%) nor Bi/Fe (atomic radii difference of 25.7%), the rest of the rules do not exclude a slight mixing between the

elements (see Table 3). Therefore, the current observations require chemical composition analysis of individual NPs to fully understand the morphological changes caused by the dopant amount.

3.2. Element composition

As indicated by ICP-MS, the Bi doping wt% increases in all samples with the employed doping salt amount, from low in the case of the $Ni_{Bi0.01}$ and $Fe_{Bi0.01}$ (3 wt% and 4 wt%, respectively) to a massive amount for the $Ni_{Bi1.00}$ and $Fe_{Bi1.00}$ (94 wt% and 72 wt%, respectively). In addition, ICP-MS results reveal that there is an abrupt composition change in the doping range of 0.1 to 1 mM, which may be an optimal zone for adjusting the composition to the maximum extent.

Table 3 Hume-Rothery rules evaluation of used elements for nanoalloys synthesis.

Rules	1.	2.	3.	4.
Element	Atomic size (nm)	Crystal structure	Electronegativity	Valency
Bi	0.156	Rhombohedral	1.9	+ III
Ni	0.1246	Cubic - FCC	1.8	+ II
Fe	0.1241	Cubic - BCC	1.8	+ II/+ III

This hypothesis is supported by additional ICP-MS measurements conducted on samples created using Bi salt solutions of 0.2, 0.4, 0.5, 0.6, and 0.8 mM (refer to Supplementary Material, Fig. S4). These measurements showed that increasing the salt amount in such a range during the synthesis allows for accurate tuning of Bi doping owing to the linear proportionality between the salt concentration and Bi doping. Additionally, EDX line scans performed on samples where structural changes can be more easily detected, i.e., the samples prepared in 0.01, 0.1, and 1.0 mM Bi solutions show that Bi can be found in all observed NPs (Fig. 4, Fig. S5, and Fig. S6 in the Supplementary Material). Therefore, complementing the observations extracted from the TEM micrograph analysis, it is possible to ratify that the elements are distributed in segregated phases within the NPs. Note that the EDX line scan analysis was performed on NPs with an average size of around 100 nm. This decision was motivated by the fact that the analysis of smaller NPs can lead to a limited collection of characteristic X-rays signal, which can introduce potential inaccuracies [37]. Therefore, the current element distribution findings only refer to the NPs with an average size of around 100 nm.

In the case of the lightly doped Ni-based samples ($Ni_{Bi0.01}$ and $Ni_{Bi0.10}$), the low Bi signal is attributed to the nanosheets covering the entire surface of Ni NPs. The Bi signal increment in the sample NiBi1.00, which exhibits a relatively homogeneous Bi signal distribution overlapping with a Ni signal displaying small peaks, denotes Ni encapsulation by Bi. This is further demonstrated by EDX maps, where the superposition of Bi and Ni atoms signal is visible even between the nested Ni and the Bi bubble-like structure. In the case of the Fe-based samples, although the EDX line scans do not indicate a core-shell structure as initially suggested by the TEM images, both element signals fluctuate significantly across the line scan. Such a fluctuation evidences an irregular mixing of Fe and Bi throughout the NPs structure, confirming that Fe NPs can incorporate the Bi dopant more efficiently. EDX mapping of the sample with the largest Bi doping ($Fe_{Bi1.00}$), on the other hand, shows a thin Bi shell barely noticeable by bright field TEM images and the incorporation of the Bi atoms into the Fe core.

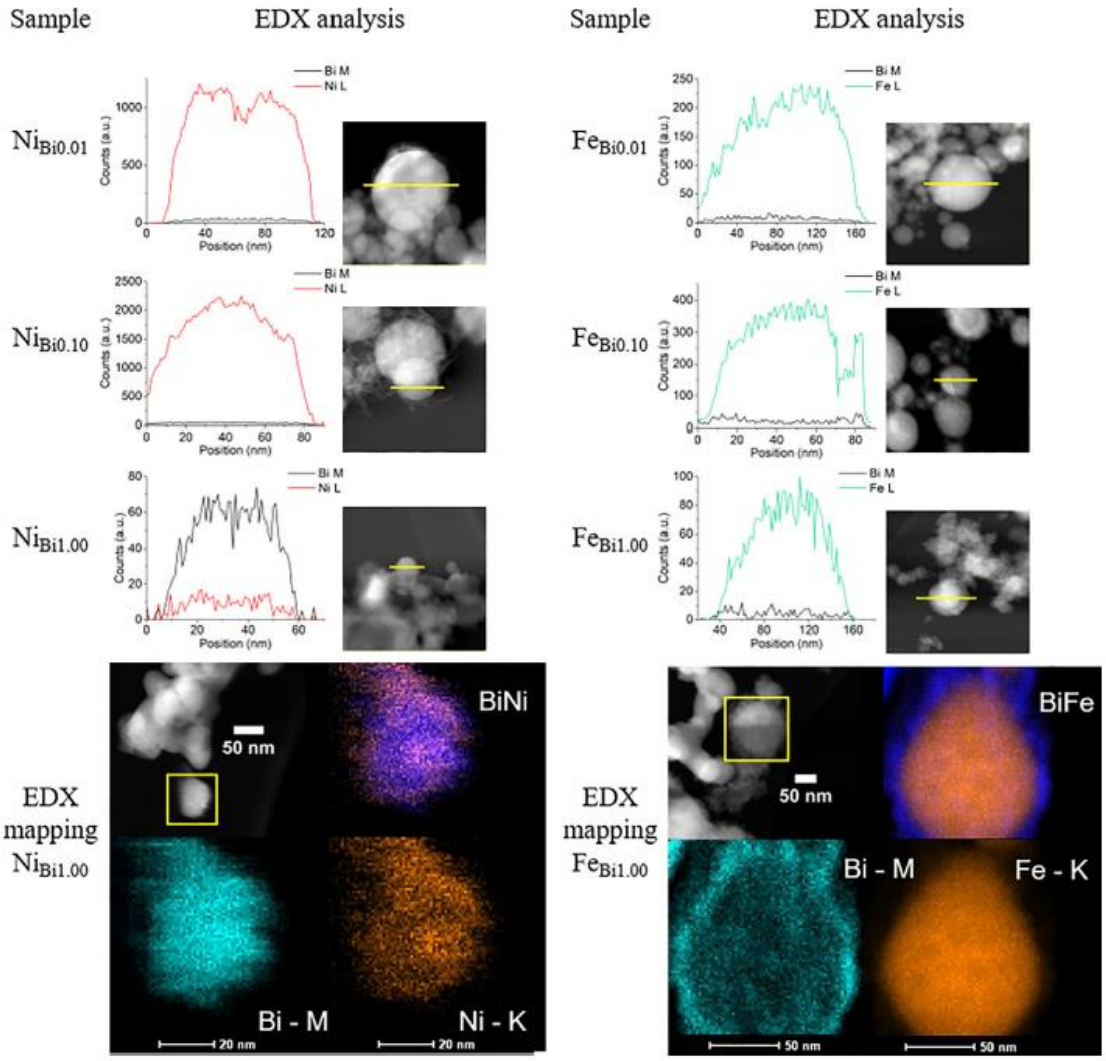

Fig. 4. EDX line scans of all the samples Indicating their elements' distribution and EDX mapping of the samples with the largest Bi doping, i.e., $Ni_{Bi1.00}$ and $Fe_{Bi1.00}$, displaying a notable phase segregation.

3.3. Phase composition

3.3.1. Individual NPs analysis

The phase segregation suggested by EDX line scan and mapping analysis can be confirmed by the HRTEM and SAED analysis (Fig. 5). Accordingly, samples $Ni_{Bi0.01}$-$Ni_{Bi1.00}$ display crystalline phases belonging to Ni and Bi, and samples $Fe_{Bi0.01}$-$Fe_{Bi1.00}$ to Fe and Bi. In the case of $Ni_{Bi0.01}$, although HRTEM analysis only shows cubic NiO (ICDD-database: 65-5745) in the NPs core, and rhombohedral Ni_3C (ICDD-database: 6-697) in their surface, SAED analysis complements these data by confirming the additional presence of cubic Ni (ICDD-database: 88-2326), monoclinic Bi (ICDD-database: 65-1215), and cubic 5-Bi_2O_3 (ICDD-database: 16-654). On the one hand, as acetone is a volatile carbon-based liquid, it can undergo molecular dissociation during its interaction with the ablation area (the laser-solid target interaction promotes the formation of a short-living plasma). This would allow the transmission of its constituent elements to the plasma and consequential incorporation into the NPs after the plasma's extinction leading to the formation of Ni carbides [13]. Moreover, since the NPs produced by RLAL are

released into the liquid immediately after their creation, they are very hot, and their contact with acetone molecules could trigger their degradation, increasing the chances of generating carbides over the NPs surface. On the other hand, the formation of bismuth sheets covering the NPs surface can be attributed to the reduction of the Bi salt over the hot NPs surface (similar to the case of acetone degradation). The plasma can trigger the acetone molecular dissociation [15], and consequent ketyl radicals generation, which can reduce the Bi salt while using the NPs surface as support. Thus, the reduced Bi salt can form metallic Bi or Bi_2O_3 polymorphs. Considering that in RLAL, the NPs ejected from the cavitation bubble hold a temperature > 1000 K for some ns [38], before rapidly decreasing, the interaction between reduced Bi species with the hot NPs surface may foster the formation of nanosheet polymorphs that are hard to get at conventional temperature transition times (~s) like 5-Bi_2O_3 (appearing at 1003-1098 K), β-Bi_2O_3 (923 K), or γ-Bi_2O_3 (912 K) [39].

Unlike the Ni-based sample, its Fe-based counterpart ($Fe_{Bi0.01}$) shows a core mainly composed of a combination of cubic Fe (ICDD-database: 85-1410), cubic FeO (ICDD-database: 77-2355) and Fe_3O_4 (ICDD-database: 79-416, 74-748), a shell formed by the same oxides, and the additional rhombohedral FeO (ICDD-database: 6-711), and no carbides. Differently from Ni, when employing laser-mediated synthesis methodologies to produce Fe NPs in acetone, Fe does not tend to form carbides, presumably due to a decomposition reaction turning the potential carbides like Fe_3C into 3Fe + C, which get rapidly oxidized [40]. SAED analysis additionally indicates the presence of rhombohedral δ-Bi_2O_3 (ICDD-database: 16-654), just as in the Ni-based counterpart, indicating that regardless of the magnetic element nature, the Bi salt follows a similar type of reduction pathway.

When increasing the Bi dopant, the Ni and Fe natures lead to very different structures. For Ni-based samples, there is an increase

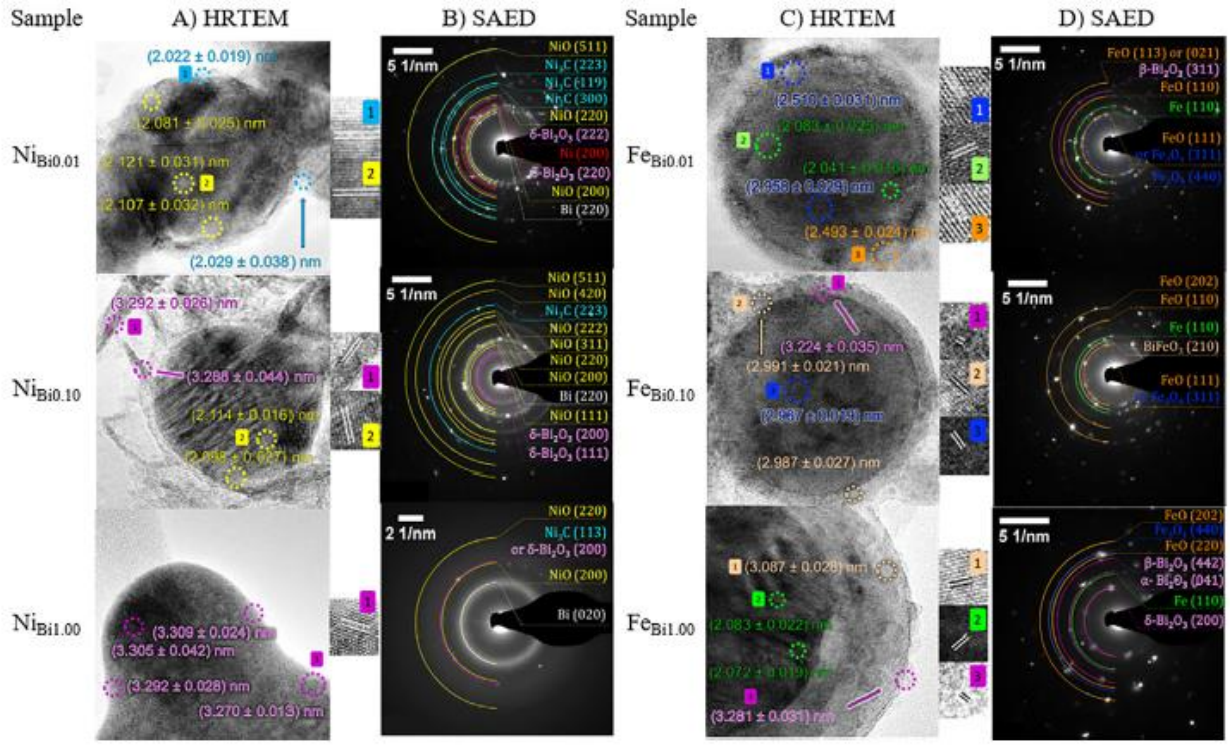

Fig. 5. The crystallographic distances found In HRTEM [(A) and (C)] Images and SAED diffraction patterns [(B) and (D)] are displayed and labeled by colors. Ni-based samples: Ni (red), NiO (yellow), Ni_3C (light blue), Bi (white), and $B_{i2}O_3$ (purple). Fe-based samples: Fe (green), FeO (orange), Fe_3O_4 (dark blue), $BiFeO_3$ (beige), and Bi_2O_3 (purple).

When increasing the Bi dopant, the Ni and Fe natures lead to very different structures. For Ni-based samples, there is an increase of δ-Bi_2O_3 while Ni_3C get heavily reduced, being only detectable by SAED. Such a result confirms the hypothesis that Bi acts as a capping agent for Ni, but the bimodal size distribution blockage is not the only outcome. The Ni_3C reduction also indicates that Bi competes with the acetone molecules to occupy the Ni-based NPs surface favoring the formation of nanosheet polymorphs like 5-Bi_2O_3. In the case of Fe-based samples, the dopant increment enables the formation of additional crystal phases such as rhombohedral $BiFeO_3$ (ICDD-database: 71-2494), monoclinic α-Bi_2O_3 (ICDD-database: 41-1449) or tetragonal δ-Bi_2O_3 (ICDD-database: 29-236). Thus, this demonstrates that an increased amount of Bi intervening in the Fe NPs formation can force the incorporation of Bi atoms within the Fe crystal resulting in phases like $BiFeO_3$. Moreover, the more significant abundance of non-nanosheet Bi_2O_3 polymorphs compared to Ni-based samples can be attributed to both elements' heat transfer difference. Similar to LAL, in the reactive version RLAL, upon condensation of the ablated material, the NPs start to shape while cooling down. During the cooling process, the heat is transferred to the surrounding liquid until thermal equilibrium is reached, triggering chemical transformations in the liquid components (solvent and solute) along the way [41]. Such transformations include thermal decomposition, vaporization, reduction/oxidation of solute and solvent molecules, and formation of reactive species [13], the extent of which will depend precisely on the NPs heat transfer [11]. Since Fe has a lower thermal conductivity than Ni [42], which affects the rate of heat transfer between the NPs and the liquid, it can be more difficult for Fe to transfer temperature fast enough to the reduced bismuth. This simultaneously favors the generation of polymorphs at lower temperatures than the 5 one and prevents an annealing effect that can benefit nanosheet formation [43].

3.3.2. Bulk analysis

The bulk XRD analysis displayed in Fig. 6, shows that the Ni-based samples exhibit the following crystalline phases, which complement the already identified phases in single particles: hexagonal alpha $Ni(OH)_2$ (ICDD-database: 22-444), hexagonal Ni_2O_3 (ICDD-database: 14-481), and rhombohedral Ni3C (ICDD-database: 6-697). Even though such peaks are clearly visible for samples Ni-$Ni_{Bi0.10}$, $Ni_{Bi1.00}$ shows no conclusive results due to its relative amount of Bi (see Table 1). Based on the TEM images, the Bi dopant not only forms crystalline phases corresponding to Bi_2O_3 polymorphs or metallic Bi but also exists in an amorphous form. This means that with an increase in the Bi dopant concentration, such as in the case of $Ni_{Bi1.00}$, the signals from these coexisting phases, which are difficult to distinguish in bulk, mask the Ni diffraction peaks. In the case of Fe-based samples, something similar occurs; the samples holding the lowest Bi concentration display the Fe-based crystalline phases corresponding to orthorhombic Fe_3O_4 (ICDD-database: 89-6466), and rhombohedral Fe_2O_3 (ICDD-database: 85-987), while the sample containing the largest amount of Bi, i.e., $Fe_{Bi1.00}$, does not show distinguishable phases. The signal shielding in $Fe_{Bi1.00}$ can be attributed, as in the case of $Ni_{Bi1.00}$, to the coexistence of Bi_2O_3 polymorphs and amorphous zones (see Fig. S8 in the Supplementary Material).

Finally, because of its ability to provide insights into metal oxide species' bond strength, length, and symmetry, even for 2D materials, Raman spectroscopy analysis adds the last complimentary details on the NPs structure [44]. As observed in Fig. 7 and summarized in Table 4, the Ni-based samples display a variety of distinct peaks that can be associated with Ni and Bi oxides. For instance, the Ni sample exhibits peaks of $Ni(OH)_2$ [45] and NiO [46-48] while the sample $NiBi_{0.01}$ has NiO peaks.

Table 4 Raman peaks presented in the Ni-based and Fe-based samples.

Compound	Peaks (cm^{-1})	Sample
$Bi(NO_3)_3$	1045, 727, 428, 263, 184, 149, 111, 86	bismuth salt
$Ni(OH)_2$	1059, 647, 266	Ni, $Ni_{Bi0.10}$
NiO	1119-1117, 1039-1029, 715, 676, 575-560, 511-504, 395-389, 361–356	Ni - $Ni_{Bi1.00}$
Bi_2O_3		
α form	532, 332, 302, 208–205, 160, 139-138, 106–105	$Ni_{Bi0.01}$ - $Ni_{Bi1.00}$, $Fe_{Bi1.00}$
β form	122, 115, 75–74	$Ni_{Bi0.01}$ - $Ni_{Bi0.10}$
δ form	630, 607	$Ni_{Bi0.10}$ - $Ni_{Bi1.00}$
Bi–O stretching	311-307, 122–121	$Ni_{Bi0.01}$ - $Ni_{Bi1.00}$, $Fe_{Bi1.00}$
Bi vibration	91, 83-81, 66-58, 52	$Ni_{Bi0.01}$ - $Ni_{Bi1.00}$ $Fe_{Bi0.10}$ - $Fe_{Bi1.00}$
Fe_2O_3		
α form	1294, 950, 623	Fe - $Fe_{Bi0.10}$
γ form	672, 495-487, 302	Fe - $Fe_{Bi0.01}$
FeO	672, 595-590, 330, 302	Fe - $Fe_{Bi0.10}$
Fe	393-390, 284-279, 218–215	$Fe_{Bi0.01}$ - $Fe_{Bi0.10}$

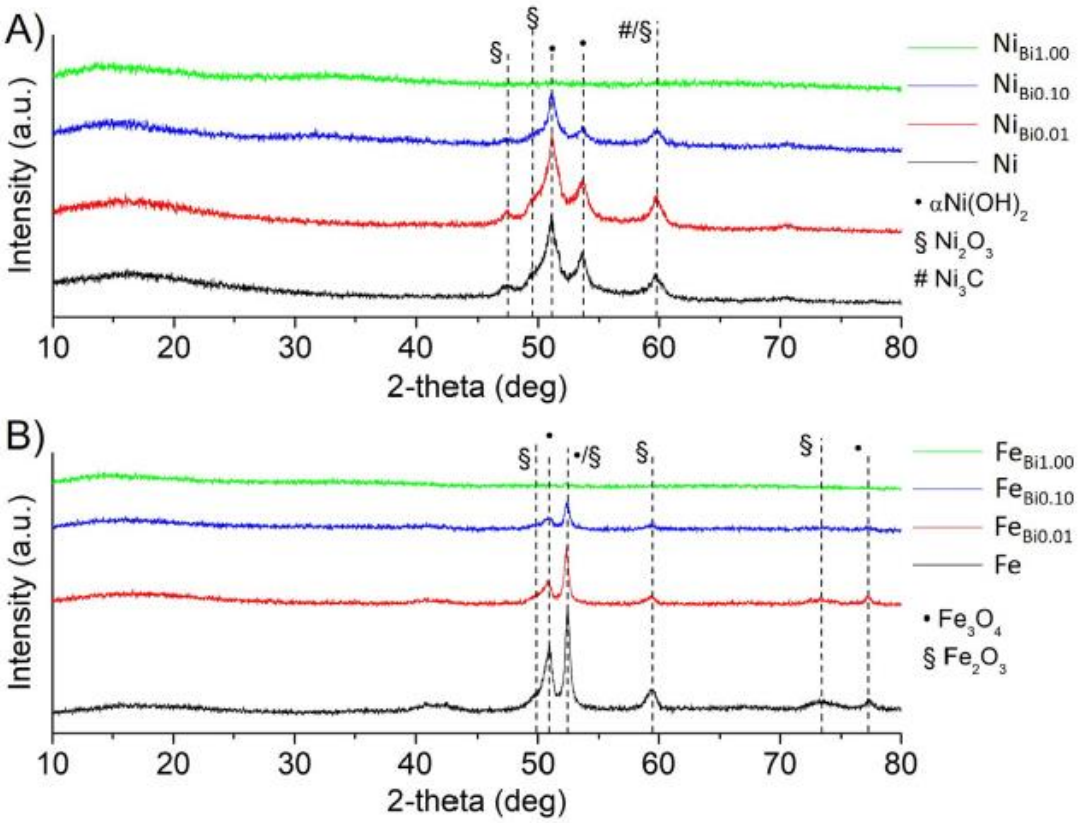

Fig. 6. XRD spectra of (A) Ni-based samples and (B) Fe-based samples indicating the identified crystalline phases.

Besides, $Ni_{Bi0.01}$ exhibits peaks of Bi_2O_3 possibly belonging to two of its forms - a and /l. [49,50] In contrast, the $Ni_{Bi0.10}$ sample shows all four mentioned phases (NiO, $Ni(OH)_2$, α-Bi_2O_3, and β-Bi_2O_3), as well as peaks attributed to δ-Bi_2O_3. Finally, the $NiBi_{1.00}$ sample exhibits Bi_2O_3 in two forms - a and 5. In addition, the spectrum shows a peak at 1039 cm^{-1}, which presumably belongs to the NiO (or alternatively to traces of residual bismuth salt). Overall, the Raman spectroscopy data suggests that the Ni-based samples contain Bi_2O_3 in three different known forms - α, β, and 5. However, the HRTEM, SAED, and XRD phase analyses indicate that the δ-Bi_2O_3 form is dominant.

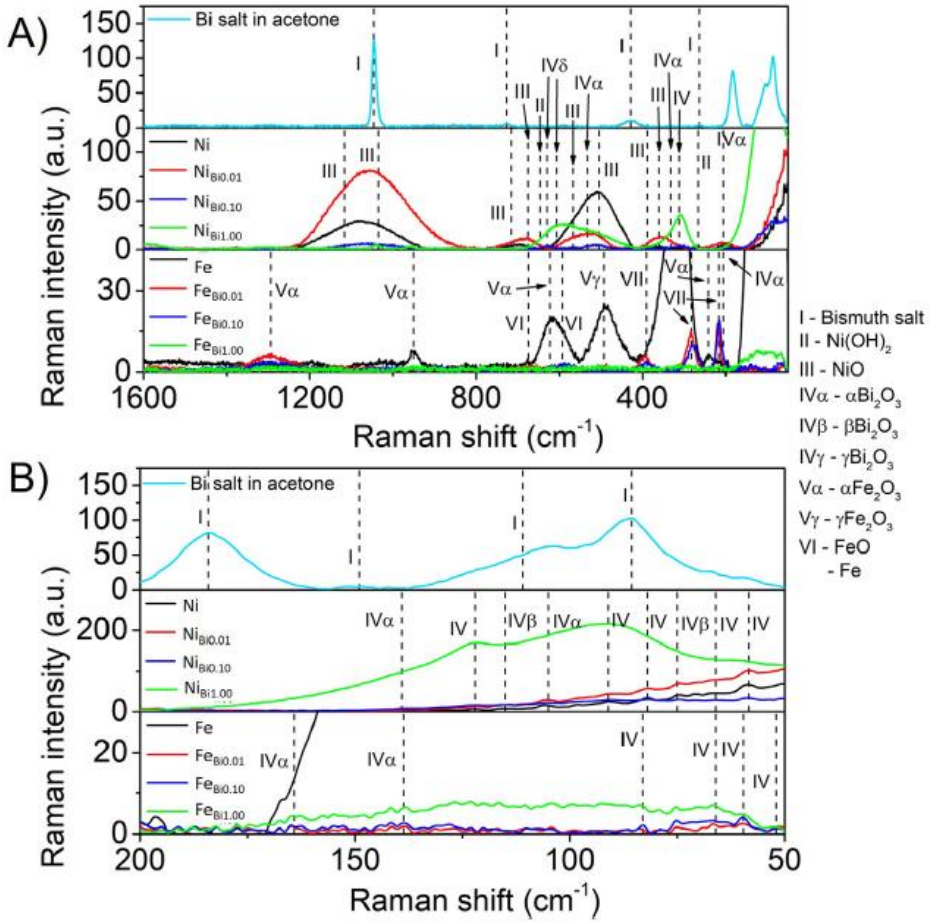

Fig. 7. Raman spectra of bismuth salt, Ni-based, and Fe-based samples, (A) in the wavenumber range 50-1600 cm^{-1} (B) in the wavenumber range 50-200 cm^{-1}

Unlike the Ni-based samples, the Fe-based ones do not start showing peaks associated with Bi oxide phases until sample $Fe_{Bi0.10}$, where a Bi salt loading of 0.1 mM was employed. The lower salt content in Fe-$Fe_{Bi0.01}$ leads to the production of Fe oxide forms like α - Fe_2O_3 (hematite), r - Fe_2O_3 (maghemite; see also Fig. S9 in the Supplementary Material), FeO (wustite), and metallic Fe [51-53]. For $Fe_{Bi0.10}$ apart from Fe phases, it is possible to observe vibration modes of Bi atom in Bi_2O_3. Sample $Fe_{Bi1.00}$, also exhibits Bi_2O_3 peaks corresponding to the vibration and stretching modes in $Bi2_{O3}$ and specific peaks for a-Bi_2O_3.

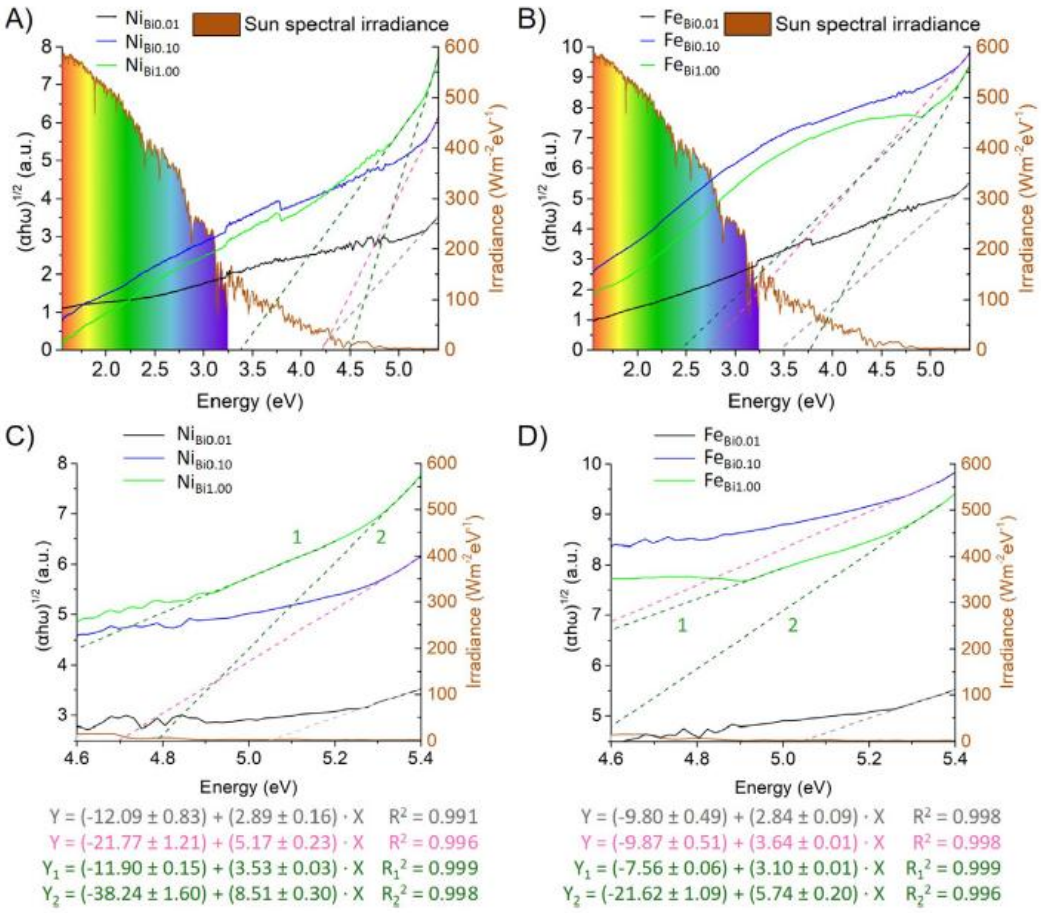

Fig. 8. Comparison between the Tauc plots of (A) Ni-based and (B) Fe-based samples with the Sun spectral irradiance during periods of moderate solar activity. Moreover, linear area magnifications of the same (C) Ni-based and (D) Fe-based samples are displayed. Note that the corresponding linear fittings are included in the pictures, and with them, their R-squared values > 0.99.

Overall, such data indicates that incrementing the Bi dopant forces its incorporation into the Fe system. For instance, the fact that Bi is observed in $Fe_{Bi0.01}$ (0.01 mM Bi salt loading) only by SAED indicates that Bi is not properly incorporated into the nanosystem, and the majority of the Bi is lost in the cleaning process. ith the salt concentration increment, Bi is more easily detected by the rest of the analytical methods indicating its incorporation into the Fe system. This reinforces the hypothesis that the Bi/Ni interaction differs from the Bi/Fe one when magnetic Bi-based nanoalloys are generated through RLAL. On the one hand, Bi behaves as a capping agent for Ni, while, on the other hand, it behaves only as a doping agent subject to internalization for Fe.

3.4. Physico-chemical properties

Since variations in the sample's phases and morphological composition have a natural impact on their physicochemical properties and suitability for real-world applications, assessing these changes in relation to the specific intended use is essential. Bi magnetic NPs were selected for their potential use as recyclable photocatalysts, so the samples' bandgap, magnetic properties, and hydrodynamic stability were analyzed.

3.4.1. Bandgap

Since semiconductors' photocatalytic properties are associated with the photogeneration of charge carriers between valence and conductive bands, the gaps between these bands (or bandgaps) need to be determined. In our current study, the samples exhibit a combination of crystalline and amorphous phases, generally resulting in tail states near the valence and conduction bands. Thus, as for the optical bandgap determination of amorphous semiconductors, it is necessary to consider that the bandgap of our samples will be defined by extrapolating the joint density of states [54]. As such, this can be easily done by employing the Tauc method, which relates the extrema of the bands to the square root of photon energy proportionally [55]. This method, also known as the Tauc plot, determines whether the bands' extremes are present in the samples, while their linear fittings show their position. As observed in Fig. 8, these data indicate that the most promising photocatalysts are those containing Fe. Unlike the Ni-based samples, the Fe-based ones show bandgap values in the 2.5-3.5 eV range despite the Bi dopant content. Such bandgap values correspond to light activation values in the longwave UV (UVA) or visible region of the electromagnetic spectrum, implying that they can benefit from a fraction of the solar spectral irradiance, which makes them more practical for efficient catalytic processes.

According to the sample's phases and morphological composition, both groups of magnetic Bi nanomaterials should be able to display photocatalytic activity, especially considering that both groups show the presence of various Bi_2O_3 polymorphs, which have bandgap values from 1.7-3.4 eV [50]. However, the interaction with the magnetic oxide elements finally determines which nanomaterial displays the most efficient bandgap shift. In the case of Ni-based samples, most of them contain NiO or Ni_2O_3 with bandgap values in the range of 3.6-4 eV [56,57], and in particular cases, getting up to 4.5 eV [58]. This results in the synergistic effect of shifting the Ni-based nanoalloys bandgap to larger values, except for $Ni_{Bi1.00}$, which has the most significant amount of Bi . This sample, in contrast, shows double bandgap values due to the more equilibrated coexistence of segregated Ni-and Bi-based crystalline phases. Although all Fe-based samples exhibit forms of Fe oxide, their bandgap values match or fall below those of the Bi_2O_3 polymorphs (1 eV for FeO, 1.9-2.2 eV for Fe_2O_3, and 1.1 eV for Fe_3O_4) [59-61]. Hence, their combination does not affect the Bi2O3 optical response, leading to the most appropriate type of magnetic Bi photocatalyst.

Additionally, in the case of the samples with the largest concentrations of Bi ($Fe_{Bi0.10}$ and $Fe_{Bi1.00}$), the dominant presence of the Bi_2O_3 polymorphs a and 5 with bandgap values 2.58-3.09 eV, and 1.73-1.95 eV, respectively [50], enables the most promising type of magnetic photocatalyst, which has the ability to be activated by light in the visible region. In the particular case of $Fe_{Bi1.00}$, the sample displays a dual bandgap as the increased concentration of Bi enables a more significant polymorphs' contribution to the final material's optical response.

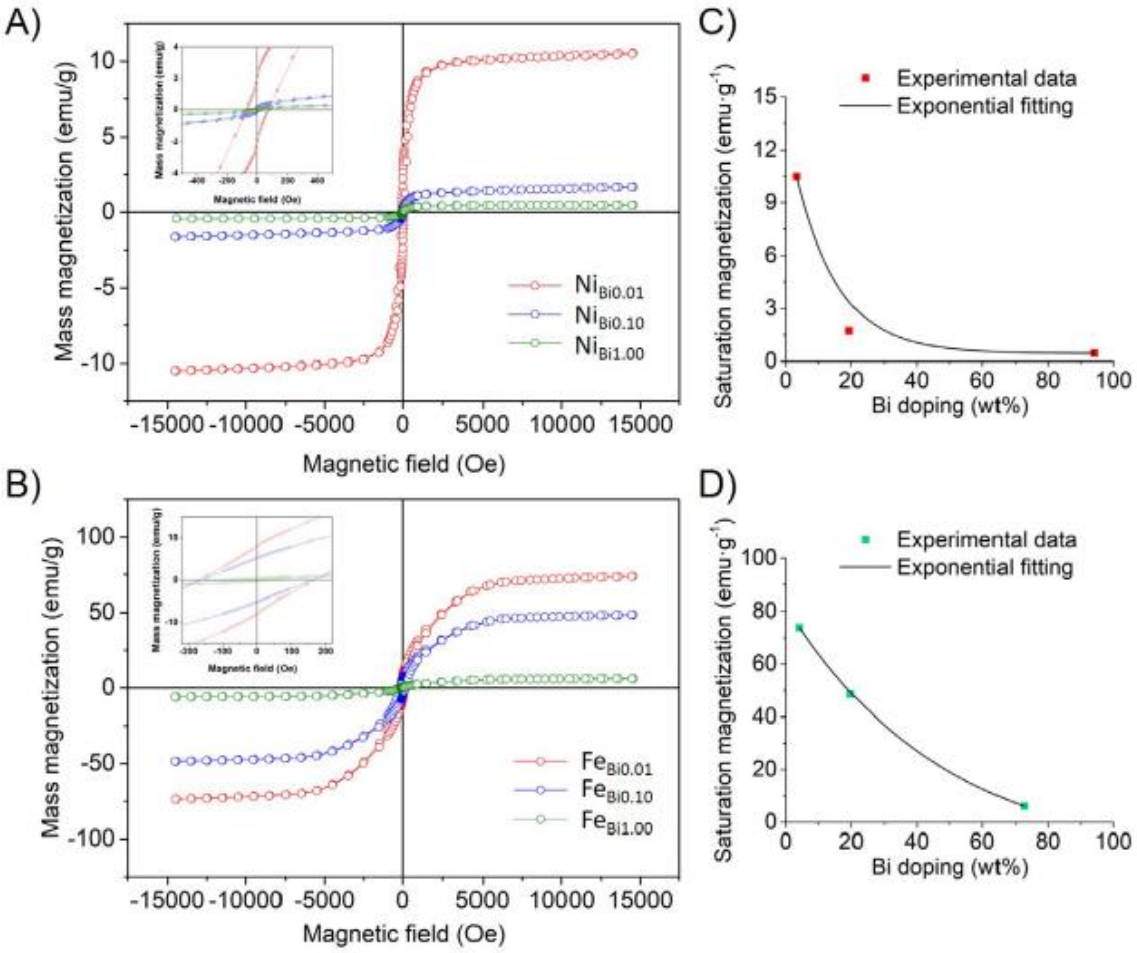

Fig. 9. Representative VSM hysteresis loops of (A) Ni-based and (B) Fe-based samples are shown with the details in the inset graphs displaying the magnification of the zero-field region. Moreover, the dependence between presented magnetic saturations and magnetic element contents are given for (C) Ni-based and (D) Fe-based samples.

3.4.2. Magnetic properties

The investigation of magnetic properties revealed that the Fe-based samples have greater potential to be used as recyclable photocatalysts (see Fig. 9A and B). Despite both groups of samples exhibiting S-shaped magnetic hysteresis loops, indicating magnetic behavior, the Fe-based samples show higher values of saturation magnetization (M_s). As observed in Fig. 9D, their M_s value gradually decreases with the amount of the Bi dopant. This observation agrees with the generally accepted fact that non-magnetic/diamagnetic compounds (e.g., Bi oxides) cause a decrease in magnetic saturation [62]. Although the same tendency is observed for the Ni-based samples, the capping effect exerted by the Bi seems to affect their magnetic response more profoundly (Fig. 9C). This phenomenon can be attributed to the spatial composition of the NPs as well as their interactions. As TEM images show (Fig. 2), the Bi-material appears to form a network around the Ni-based NPs, preventing their growth, forming veils for $Ni_{Bi0.10}$, and encapsulating bubbles for $Ni_{Bi1.00}$. Typically, the magnetic properties of NPs scale as their size increases. In the case of the Ni-based NPs, the growth hinders their magnetic response [63]. Moreover, the presence of Bi oxides yields a higher interparticle spacing between the adjacent NPs, suppressing the collective magnetization. Such an elemental ordering in the Ni-based

NPs adds a disadvantage, as a region at the surface or interface with the substrate likely produces magnetic dead layers (MDLs), further contributing to the overall reduction of magnetic behavior [64].

Table 5 Magnetic parameters of the synthesized NPs.

Sample	M_R (emu g^{-1})	H_C (Oe)	M_S (emu g^{-1})	M_R/M_S (a.u.)	K (emu Oe g^{-1})
$Ni_{Bi0.01}$	2.0	76	10.5	0.190	814
$Ni_{Bi0.10}$	0.15	17	1.7	0.088	29.5
$Ni_{Bi1.00}$	0.05	20	0.45	0.111	9.2
$Fe_{Bi0.01}$	8.0	166	73.8	0.108	12496
$Fe_{Bi0.10}$	5.2	163	48.5	0.107	8064
$Fe_{Bi1.00}$	0.4	45	6.1	0.066	280

The magnetic saturation, magnetic coercivity, remanent magnetization, remanence ratio, and anisotropy constant values are determined from the hysteresis loops and summarized in Table 5. The calculation of the anisotropy constants is based on the theory of Stoner and Wohlfarth [15], applying the formula:

$$K = 1.02 \cdot H_c \cdot M_s \qquad (2)$$

where K represents the anisotropy constant, H_c coercivity, and M_s magnetic saturation of the sample.

In line with the magnetization saturation values, coercivity and anisotropy decrease as the Bi doping increases in either group of samples. Such a tendency indicates that, although these values correspond to soft magnetic materials [65], their response to magnetic fields can be modulated with the Bi dosage. Thus, as the Bi dosage increases, the materials' resistance to changing magnetization and the alignment of their total magnetic moments decrease. Considering these results and the bandgap calculations, it can be concluded that Fe-based samples are more appropriate for use as recyclable photocatalysts. Furthermore, as proved by ICP-OES data, even at low wt%, Fe can impart adequate magnetic properties to recycle photocatalysts that benefit from the light's visible spectral range.

3.4.3. Stability

While the magnetic properties and optical bandgap are undoubtedly the most crucial parameters that affect the samples' efficacy as recyclable photocatalysts, it is also essential to have high hydrodynamic stability during the catalytic reactions to guarantee a consistent and stable performance. Therefore, the NPs' hydrodynamic stability (Fig. 10A and B) was tested by UV-Vis spectroscopy and zeta potential measurements after their transfer into demineralized water as its use is more common when employing Bi-based nanomaterials as heterogeneous photocatalysts [66]. Note that as the zeta potential electrokinetic model is designed for spherical NPs dispersed in solvents with well-known parameters, the values obtained for our non-spherical NPs dispersed in water containing traces of acetone and its degradation products derived from the cleaning process can be inaccurate; hence, such data should be considered solely as a qualitative superficial charge change observation rather than quantitative.

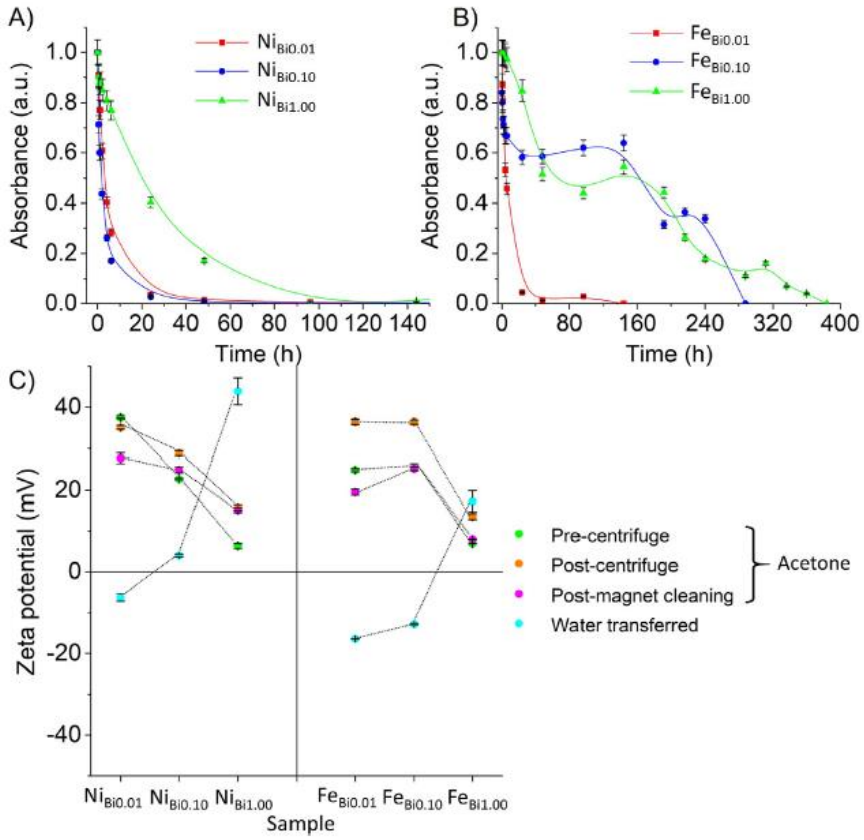

Fig. 10. Time evolution of absorbance in (A) Ni-based and (B) Fe-based samples indicating their hydrodynamic stability in the water, which is supplemented by the (C) zeta potentials through all states of cleaning process.

In general, the samples' absorbance evolution through time (394 nm for Ni-based samples [67] and 348 nm for Fe-based ones [68]) are not very promising as most samples do not withstand beyond six days, except for samples $Fe_{Bi0.01}$ and $Fe_{Bi1.00}$, which can stay stable for two additional days. The stability analysis, however, provides additional information, showing that, in general, Bi-doping positively impacts the NPs hydrodynamic stability. As reported elsewhere, the Bi dopant alters Ni [69] and Fe [70] crystalline lattices, and in particular [Bi^{3+}] interaction at the NPs surface can neutralize or totally change the NPs superficial charge as demonstrated by the zeta potential measurements displayed in Fig. 10C, leading to an electrostatically-driven stability increment. As water displays extensive ion solvation capabilities, this aspect can improve the distribution of charges on the NPs surface [71], resulting in a more pronounced superficial charge change in comparison to samples dispersed in acetone, which only displays a slight superficial charge modification as a consequence of non-consumed Bi salt remotion during the cleaning process stages. Since no additional ligand was employed to stabilize these NPs, further electrical double layer modification by, for instance, the incorporation of monovalent salts in the liquid medium, can serve as a stabilization mechanism. Therefore, stable nanocolloids can be obtained while keeping the NPs maximum number of potential active sites free, resulting in optimal photocatalytic performance.

4. Conclusion

In summary, the current manuscript unveils new limitations and opportunities for RLAL. It evidences that while two elements may have extremely similar physicochemical properties, using each one separately to produce nanoalloys with a photocatalytic element can significantly impact the final composition, morphology, and overall photocatalytic behavior of the resulting nanoalloys. This is used to our advantage by controlling the design of nanoalloys based on a magnetic element (nickel or iron) and bismuth. The controlled atoms-structuring in the nanoalloys enables us to modify the nanoalloys' bandgap and magnetic saturation. Moreover, owing to the employment of various amounts of bismuth dosage, a group of diverse potential photocatalysts, with the ability to be up to 99% magnetically recovered, is synthesized.

In the case of the Ni-based samples, different polymorphs of Bi_2O_3 act as a capping agent, either wrapping the surface of various Ni oxides and carbide NPs or completely encapsulating them in nanobubbles comprising a combination of the said polymorphs and a Bi-based amorphous structure as the Bi dosage increases. In contrast, when it comes to the Fe-based samples, incrementing the Bi dosage leads to the internalization of Bi into various Fe oxide NPs, resulting in the creation of bimetallic oxide phases, such as $BiFeO_3$ at the maximum Bi dosage. Interestingly, this phenomenon occurs even though the Hume-Rothery rules suggest that these two elements should not form homogeneous nanoalloys. However, as the ablated materials' heat transfer seem to play a fundamental role in incorporating Bi into the internal NPs structure while the NPs freeze, such materials' characteristic that happens to vary depending on the element allows the formation of nanostructures with radically different properties. For instance, the Bi incorporation into the Fe-based nanosystems results in the bandgap shifting of Bi_2O_3 polymorphs extending into the visible and UVA light regions. Furthermore, even though the magnetic properties of Ni- and Fe-based nanomaterials decrease due to Bi doping, they remain strong enough to provide magnetophoretic motility to the photocatalysts. Additionally, as these NPs are ligand-free, stabilizing them through electrical double layer modification can create magnetically recyclable photocatalysts capable of being activated by visible light and possessing the maximum possible number of active sites. Overall, the fine control of nanoalloys achieved in this study by exploring the limits of the sustainable laser-mediated RLAL method presents a promising prospect in the field of recyclable photocatalysis.

References

[1] M.C. Roco, Overview: Affirmation of nanotechnology between 2000 and 2030, Nanotechnol. Commer.: Manuf. Process. Prod. (2017) 1-23, http://dx.doi.org/ 10.1002/9781119371762.CH1.

[2] A. Reverberi, N. Kuznetsov, V. Meshalkin, M. Salerno, B. Fabiano, Systematical analysis of chemical methods in metal nanoparticles synthesis, Theor. Found. Chem. Eng. 50 (1) (2016) 59-66, http://dx.doi.org/10.1134/ S0040579516010127.

[3] A. Nikam, B. Prasad, A. Kulkarni, Wet chemical synthesis of metal oxide nanoparticles: A review, CrystEngComm 20 (35) (2018) 5091-5107, http://dx. doi.org/10.1039/C8CE00487K.

[4] T.K. Barik, G.C. Maity, P. Gupta, L. Mohan, T.S. Santra, Nanomaterials: an introduction, in: Nanomaterials and their Biomedical Applications, Springer, 2021, pp. 1-27, http://dx.doi.org/10.1007/978-981-33-6252-9_1.

[5] F. Ahmad, Q. Saeed, S.M.U. Shah, M.A. Gondal, S. Mumtaz, Environmental sustainability: challenges and approaches, Natural Resour. Conserv. Adv. Sustain. (2022) 243-270, http://dx.doi.org/10.1016/B978-0-12-822976-7.00019-3.

[6] N. Jan, N. Majeed, M. Ahmad, W.A. Lone, R. John, Nano-pollution: Why it should worry us, Chemosphere (2022) 134746, http://dx.doi.org/10.1016/j. chemosphere.2022.134746.

[7] P. Kumar, S. Dua, R. Kaur, M. Kumar, G. Bhatt, A review on advancements in carbon quantum dots and their application in photovoltaics, RSC Adv. 12 (8) (2022) 4714-4759, http://dx.doi.org/10.1039/D1RA08452F.

[8] H. Nadaroglu, A.A. GUNGOR, i. Selvi, Synthesis of nanoparticles by green synthesis method, Int. J. Innov. Res. Rev. 1 (1) (2017) 6-9, http://www.injirr. com/index.php/injirr/article/view/4.

[9] K. Pal, S. Chakroborty, N. Nath, Limitations of nanomaterials insights in green chemistry sustainable route: Review on novel applications, Green Process. Synth. 11 (1) (2022) 951-964, http://dx.doi.org/10.1515/gps-2022-0081.

[10] R. Ferrando, J. Jellinek, R.L. Johnston, Nanoalloys: from theory to applications of alloy clusters and nanoparticles, Chem. Rev. 108 (3) (2008) 845-910, http: //dx.doi.org/10.1021/cr040090g.

[11] D. Zhang, B. Gokce, S. Barcikowski, Laser synthesis and processing of colloids: fundamentals and applications, Chem. Rev. 117 (5) (2017) 3990-4103, http: //dx.doi.org/10.1021/acs.chemrev.6b00468.

[12] D. Amans, W. Cai, S. Barcikowski, Status and demand of research to bring laser generation of nanoparticles in liquids to maturity, Appl. Surf. Sci. 488 (2019) 445-454, http://dx.doi.org/10.1016/j.apsusc.2019.05.117.

[13] L.M. Frias Batista, A. Nag, V.K. Meader, K.M. Tibbetts, Generation of nanomaterials by reactive laser-synthesis in liquid, Sci. China Phys., Mech. Astron. 65 (7) (2022) 1-45, http://dx.doi.org/10.1007/s11433-021-1835-x.

[14] W.D. Callister, D.G. Rethwisch, et al., Materials Science and Engineering: An Introduction, Vol. 9, Wiley New York, 2018.

[15] R. Torres-Mendieta, O. Havelka, M. Urbánek, M. Cvek, S. Wacfawek, V.V.T. Padil, D. Jašíková, M. Kotek, M. Černík, Laser-assisted synthesis of Fe-Cu oxide nanocrystals, Appl. Surf. Sci. 469 (2019) 1007-1015, http://dx.doi.org/10.1016/ j.apsusc.2018.11.058.

[16] J. Johny, M. Kamp, O. Prymak, A. Tymoczko, U. Wiedwald, C. Rehbock, U. Schurmann, R. Popescu, D. Gerthsen, L. Kienle, et al., Formation of Co-Au coreshell nanoparticles with thin gold shells and soft magnetic e-cobalt cores ruled by thermodynamics and kinetics, J. Phys. Chem. C 125 (17) (2021) 9534—9549, http://dx.doi.org/10.1021/acs.jpcc.1c02138.

[17] A. Nag, C.M. Nguyen, K.M. Tibbetts, Heterogeneous to homogeneous Cu-Ag nanoparticles by laser reduction in liquid, Appl. Surf. Sci. 610 (2023) 155384, http://dx.doi.org/10.1016/j.apsusc.2022.155384.

[18] J. Johny, O. Prymak, M. Kamp, F. Calvo, S.-H. Kim, A. Tymoczko, A. El-Zoka, C. Rehbock, U. Schurmann, B. Gault, L. Kienle, S. Barcikowski, Multidimensional thermally-induced transformation of nest-structured complex Au-Fe nanoalloys towards equilibrium, Nano Res. 15 (1) (2022) 581-592, http://dx.doi.org/10. 1007/s12274-021-3524-7.

[19] V. Amendola, I.D. Amans, Y. Ishikawa, N. Koshizaki, S. Scire, G. Compagnini, S. Reichenberger, I.S. Barcikowski, Room-temperature laser synthesis in liquid of oxide, metal-oxide core-shells, and doped oxide nanoparticles, Chemistry (Weinheim an der Bergstrasse, Germany) 26 (42) (2020) 9206, http://dx.doi. org/10.1002/chem.202000686.

[20] V. Torresan, D. Forrer, A. Guadagnini, D. Badocco, P. Pastore, M. Casarin, A. Selloni, D. Coral, M. Ceolin, M.B. Fernandez van Raap, et al., 4D multimodal nanomedicines made of nonequilibrium Au-Fe alloy nanoparticles, ACS Nano 14 (10) (2020) 12840-12853, http://dx.doi.org/10.1021/acsnano.0c03614.

[21] D. Ettel, O. Havelka, S. Isik, D. Silvestri, S. Wacfawek, M. Urbánek, V.V. Padil, M. Černík, F. Yalcinkaya, R. Torres-Mendieta, Laser-synthesized Ag/TiO nanoparticles to integrate catalytic pollutant degradation and antifouling enhancement in nanofibrous membranes for oil-water separation, Appl. Surf. Sci. 564 (2021) 150471, http://dx.doi.org/10.1016/j.apsusc.2021.150471.

[22] R. Torres-Mendieta, N.H. Nguyen, A. Guadagnini, J. Semerad, D. Lukowiec, P. Parma, J. Yang, S. Agnoli, A. Sevcu, T. Cajthaml, et al., Growth suppression of bacteria by biofilm deterioration using silver nanoparticles with magnetic doping, Nanoscale 14 (48) (2022) 18143-18156, http://dx.doi.org/10.1039/ D2NR03902H.

[23] R. Brandiele, A. Guadagnini, L. Girardi, G. Dražíc, M.C. Dalconi, G.A. Rizzi, V. Amendola, C. Durante, Climbing the oxygen reduction reaction volcano plot with laser ablation synthesis of pt x y nanoalloys, Catal. Sci. Technol. 10 (14) (2020) 4503-4508, http://dx.doi.org/10.1039/D0CY00983K.

[24] A. Guadagnini, S. Agnoli, D. Badocco, P. Pastore, D. Coral, M.B.F. van Raap, D. Forrer, V. Amendola, Facile synthesis by laser ablation in liquid of nonequilibrium cobalt-silver nanoparticles with magnetic and plasmonic properties, J. Colloid Interface Sci. 585 (2021) 267-275, http://dx.doi.org/10.1016/j.jcis.2020. 11.089.

[25] M. Ma, Y. Chen, Z. Tong, Y. Liu, Y. Ma, R. Wang, Y. Bi, Z. Liao, Research progress of magnetic bismuth-based materials in photocatalysis: A review, J. Alloys Compd. 886 (2021) 161096, http://dx.doi.org/10.1016/j.jallcom.2021.161096.

[26] S. Siebeneicher, F. Waag, M. Escobar Castillo, V.V. Shvartsman, D.C. Lupascu, B. Gokce, Laser fragmentation synthesis of colloidal bismuth ferrite particles, Nanomaterials 10 (2) (2020) 359, http://dx.doi.org/10.3390/nano10020359.

[27] B.E. Murdock, K.E. Toghill, N. Tapia-Ruiz, A perspective on the sustainability of cathode materials used in lithium-ion batteries, Adv. Energy Mater. 11 (39) (2021) 2102028, http://dx.doi.org/10.1002/aenm.202102028.

[28] N. Karthi, K. Ramesh Kumar, P. Maadeswaranc, Pristine and nickel doped bismuth vanadate nanopowder for p-nitrophenol degradation under UV light irradiation, Egypt. J. Chem. 65 (4) (2022) 1-7, http://dx.doi.org/10.21608/ EJCHEM.2021.77859.3812.

[29] E. Struleva, S. Ashitkov, P. Komarov, K. Khishchenko, M. Agranat, Strength of iron melt at high extension rate during femtosecond laser ablation, J. Phys.: Conf. Ser. 774 (2016) 012098, http://dx.doi.org/10.1088/1742-6596/774/1/012098.

[30] S. Amoruso, R. Bruzzese, X. Wang, N. Nedialkov, P. Atanasov, Femtosecond laser ablation of nickel in vacuum, J. Phys. D: Appl. Phys. 40 (2) (2007) 331, http://dx.doi.org/10.1088/0022-3727/40/2/008.

[31] C. Cheng, X. Xu, Mechanisms of decomposition of metal during femtosecond laser ablation, Phys. Rev. B 72 (16) (2005) 165415, http://dx.doi.org/10.1103/ PhysRevB.72.165415.

[32] C.-Y. Shih, R. Streubel, J. Heberle, A. Letzel, M.V. Shugaev, C. Wu, M. Schmidt, B. Gokce, S. Barcikowski, L.V. Zhigilei, Two mechanisms of nanoparticle generation in picosecond laser ablation in liquids: the origin of the bimodal size distribution, Nanoscale 10 (15) (2018) 6900-6910, http://dx.doi.org/10.1039/C7NR08614H.

[33] R. Tilaki, A. Iraji Zad, S. Mahdavi, Stability, size and optical properties of silver nanoparticles prepared by laser ablation in different carrier media, Appl. Phys. A 84 (2006) 215-219, http://dx.doi.org/10.1007/s00339-006-3604-2.

[34] M.-R. Kalus, N. Barsch, R. Streubel, E. Gokce, S. Barcikowski, B. Gokce, How persistent microbubbles shield nanoparticle productivity in laser synthesis of colloids-quantification of their volume, dwell dynamics, and gas composition, Phys. Chem. Chem. Phys. 19 (10) (2017) 7112-7123, http://dx.doi.org/10.1039/ C6CP07011F.

[35] M.G. John, K.M. Tibbetts, One-step femtosecond laser ablation synthesis of sub-3 nm gold nanoparticles stabilized by silica, Appl. Surf. Sci. 475 (2019) 1048-1057, http://dx.doi.org/10.1016/j.apsusc.2019.01.042.

[36] N.B. Alsharif, S. Muráth, B. Katana, I. Szilagyi, Composite materials based on heteroaggregated particles: Fundamentals and applications, Adv. Colloid Interface Sci. 294 (2021) 102456, http://dx.doi.org/10.1016/j.cis.2021.102456.

[37] Y. Han, J. Jang, E. Cha, J. Lee, H. Chung, M. Jeong, T.-G. Kim, B.G. Chae, H.G. Kim, S. Jun, et al., Deep learning STEM-EDX tomography of nanocrystals, Nat. Mach. Intell. 3 (3) (2021) 267-274, http://dx.doi.org/10.1038/s42256-020-00289-5.

[38] L. Rayleigh, VIII. On the pressure developed in a liquid during the collapse of a spherical cavity, London, Edinburgh, Dublin Philos. Mag. J. Sci. 34 (200) (1917) 94-98, http://dx.doi.org/10.1080/14786440808635681.

[39] H. Sudrajat, P. Sujaridworakun, Low-temperature synthesis of á-Bi2O3 hierarchical nanostructures composed of ultrathin nanosheets for efficient photocatalysis, Mater. Des. 130 (2017) 501-511, http://dx.doi.org/10.1016/j.matdes.2017.05. 087.

[40] D. Zhang, C. Zhang, J. Liu, Q. Chen, X. Zhu, C. Liang, Carbon-encapsulated metal/metal carbide/metal oxide core-shell nanostructures generated by laser ablation of metals in organic solvents, ACS Appl. Nano Mater. 2 (1) (2018) 28-39, http://dx.doi.org/10.1021/acsanm.8b01541.

[41] N. Inogamov, V. Zhakhovsky, V.A. Khokhlov, Physical processes accompanying laser ablation in liquid, JETP Lett. 115 (1) (2022) 16-22, http://dx.doi.org/10. 1134/S002136402201009X.

[42] Y.S. Touloukian, Thermal conductivity-metallic elements and alloys, Thermophys. Prop. Matter 1 (1970) https://www.osti.gov/biblio/5447756.

[43] Z. Zhao, Y. Lin, J. Wu, J. Li, M. Lei, Mixed-phase cobalt-based nanosheets prepared by rapid thermal annealing for oxygen evolution catalysis, Adv. Compos. Hybrid Mater. 5 (3) (2022) 2589-2600, http://dx.doi.org/10.1007/s42114-022-00537-9.

[44] K. Nakamoto, Infrared and Raman Spectra of Inorganic and Coordination Compounds, Part B: Applications in Coordination, Organometallic, and Bioinorganic Chemistry, John Wiley & Sons, 2009, http://dx.doi.org/10.1002/ 9780470405888.

[45] D.S. Hall, D.J. Lockwood, S. Poirier, C. Bock, B.R. MacDougall, Raman and infrared spectroscopy of a and f phases of thin nickel hydroxide films electrochemically formed on nickel, J. Phys. Chem. A 116 (25) (2012) 6771-6784, http://dx.doi.org/10.1021/jp303546r.

[46] E. Aytan, B. Debnath, F. Kargar, Y. Barlas, M. Lacerda, J. Li, R. Lake, J. Shi, A. Balandin, Spin-phonon coupling in antiferromagnetic nickel oxide, Appl. Phys. Lett. 111 (25) (2017) 252402, http://dx.doi.org/10.1063/1.5009598.

[47] J. Roblero, F. Pola-Albores, M. Valenzuela, E. Rojas-García, E. Ríos-Valdovinos, G. Valverde-Aguilar, Ni and Ni3C catalysts supported on mesoporous silica for dry reforming of methane, Int. J. Hydrogen Energy 44 (21) (2019) 10473-10483, http://dx.doi.org/10.1016/j.ijhydene.2019.02.119.

[48] N. Mironova-Ulmane, A. Kuzmin, I. Steins, J. Grabis, I. Sildos, M. Pars, Raman scattering in nanosized nickel oxide NiO, J. Phys.: Conf. Ser. 93 (2007) 012039, http://dx.doi.org/10.1088/1742-6596/93/1/012039.

[49] C. Díaz-Guerra, P. Almodóvar, M. Camacho-Lopez, S. Camacho-López, J. Pi-queras, Formation of ^-Bi2O3 and á-Bi2O3 during laser irradiation of bi films studied in-situ by spatially resolved Raman spectroscopy, J. Alloys Compd. 723 (2017) 520-526, http://dx.doi.org/10.1016/j.jallcom.2017.06.263.

[50] C.-C. Yu, H. Chang, A.-C. Sun, J.-W. Chiou, Stabilization of the ^-phase Bi2O3 (201) thin film by an ultrathin Bi (001) seeding layer, Vacuum 169 (2019) 108918, http://dx.doi.org/10.1016/j.vacuum.2019.108918.

[51] A. Liu, J. Liu, W.-x. Zhang, Transformation and composition evolution of nanoscale zero valent iron (nZVI) synthesized by borohydride reduction in static water, Chemosphere 119 (2015) 1068-1074, http://dx.doi.org/10.1016/ j.chemosphere.2014.09.026.

[52] A. Liu, J. Liu, J. Han, W.-x. Zhang, Evolution of nanoscale zero-valent iron (nZVI) in water: Microscopic and spectroscopic evidence on the formation of nano-and micro-structured iron oxides, J. Hazard. Mater. 322 (2017) 129-135, http://dx.doi.org/10.1016/j.jhazmat.2015.12.070.

[53] M. Hanesch, Raman spectroscopy of iron oxides and (oxy) hydroxides at low laser power and possible applications in environmental magnetic studies, Geophys. J. Int. 177 (3) (2009) 941-948, http://dx.doi.org/10.1111/j.1365-246X.2009. 04122.x.

[54] A.R. Zanatta, Revisiting the optical bandgap of semiconductors and the proposal of a unified methodology to its determination, Sci. Rep. 9 (1) (2019) 11225, http://dx.doi.org/10.1038/s41598-019-47670-y.

[55] J. Tauc, R. Grigorovici, A. Vancu, Optical properties and electronic structure of amorphous germanium, Phys. Status Solidi (B) 15 (2) (1966) 627-637, http://dx.doi.org/10.1002/pssb.19660150224.

[56] H. Yang, Q. Tao, X. Zhang, A. Tang, J. Ouyang, Solid-state synthesis and electrochemical property of SnO2/NiO nanomaterials, J. Alloys Compd. 459 (1-2) (2008) 98-102, http://dx.doi.org/10.1016/j.jallcom.2007.04.258.

[57] Z.N. Kayani, S. Riaz, S. Naseem, R. Zia, Synthesis and characterization of Ni2O3 thin films, ACEM16, Jeju, South Korea (2016) https://api.semanticscholar.org/ CorpusID:220704966.

[58] C. Noguera, W. Mackrodt, Ab initio study of ground and excited states of NiO (100) monolayer, J. Phys.: Condens. Matter 12 (10) (2000) 2163, http: //dx.doi.org/10.1088/0953-8984/12/10/303.

[59] F. Schrettle, C. Kant, P. Lunkenheimer, F. Mayr, J. Deisenhofer, A. Loidl, Wustite: electric, thermodynamic and optical properties of FeO, Eur. Phys. J. B 85 (2012) 1-12, http://dx.doi.org/10.1140/epjb/e2012-30201-5.

[60] O. Seo, A. Tayal, J. Kim, C. Song, Y. Chen, S. Hiroi, Y. Katsuya, T. Ina, O. Sakata, Y. Ikeya, et al., Tuning of structural, optical band gap, and electrical properties of room-temperature-grown epitaxial thin films through the Fe2O3: NiO ratio, Sci. Rep. 9 (1) (2019) 4304, http://dx.doi.org/10.1038/s41598-019-41049-9.

[61] Y.-h. Zheng, Y. Cheng, F. Bao, Y.-s. Wang, Synthesis and magnetic properties of Fe3O4 nanoparticles, Mater. Res. Bull. 41 (3) (2006) 525-529, http://dx.doi. org/10.1016/j.materresbull.2005.09.015.

[62] R.S. Yadav, I. Kuřitka, J. Vilcakova, J. Havlica, L. Kalina, P. Urbánek, M. Machovsky, M. Masař, M. Holek, Influence of La 3+ on structural, magnetic, dielectric, electrical and modulus spectroscopic characteristics of single phase CoFe 2- x La x O 4 nanoparticles, J. Mater. Sci., Mater. Electron. 28 (12) (2017) 9139-9154, http://dx.doi.org/10.1007/s10854-017-6648-5.

[63] E.D. Smolensky, H.-Y.E. Park, Y. Zhou, G.A. Rolla, M. Marjańska, M. Botta, V.C. Pierre, Scaling laws at the nanosize: the effect of particle size and shape on the magnetism and relaxivity of iron oxide nanoparticle contrast agents, J. Mater. Chem. B 1 (22) (2013) 2818-2828, http://dx.doi.org/10.1039/C3TB00369H.

[64] A.A. Shafe, M.D. Hossain, R.A. Mayanovic, V. Roddatis, M. Benamara, Tuning exchange coupling in nio-based bimagnetic heterostructured nanocrystals, ACS Appl. Mater. Interfaces 13 (20) (2021) 24013-24023, http://dx.doi.org/10.1021/ acsami.1c02855.

[65] A. Inoue, F. Kong, Soft magnetic materials, in: A.-G. Olabi (Ed.), Encyclopedia of Smart Materials, Elsevier, Oxford, 2022, pp. 10-23, http://dx.doi.org/10.1016/ B978-0-12-803581-8.11725-4.

[66] G. Li, B. Wang, D.E. Resasco, Water-mediated heterogeneously catalyzed reactions, ACS Catal. 10 (2) (2019) 1294-1309, http://dx.doi.org/10.1021/acscatal. 9b04637.

[67] M. Malik, K.H. Chan, G. Azimi, Quantification of nickel, cobalt, and manganese concentration using ultraviolet-visible spectroscopy, RSC Adv. 11 (45) (2021) 28014-28028, http://dx.doi.org/10.1039/D1RA03962H.

[68] M. Torras, C. Moya, G.A. Pasquevich, A. Roig, Accurate iron quantification in colloids and nanocomposites by a simple UV-vis protocol, Microchim. Acta 187 (2020) 1-10, http://dx.doi.org/10.1007/s00604-020-04454-w.

[69] P.B. Koli, S.G. Shinde, K.H. Kapadnis, A.P. Patil, M.P. Shinde, S.D. Khairnar, D.B. Sonawane, R.S. Ingale, Transition metal incorporated, modified bismuth oxide (Bi2O3) nano photo catalyst for deterioration of rosaniline hydrochloride dye as resource for environmental rehabilitation, J. Indian Chem. Soc. 98 (11) (2021) 100225, http://dx.doi.org/10.10Wj.jics.2021.100225.

[70] Y. Zhu, J. Xue, T. Xu, G. He, H. Chen, Enhanced photocatalytic activity of magnetic core-shell Fe 3 O 4@ Bi 2 O 3-RGO heterojunctions for quinolone antibiotics degradation under visible light, J. Mater. Sci., Mater. Electron. 28 (2017) 8519-8528, http://dx.doi.org/10.1007/ s10854-017-6574-6.

[71] P. Siani, G. Frigerio, E. Donadoni, C. Di Valentin, Modeling zeta potential for nanoparticles in solution: Water flexibility matters, J. Phys. Chem. C (2023) http://dx.doi.org/10.1021/acs.jpcc.2c08988.